Journal of Materials Chemistry A

ROYAL SOCIETY OF CHEMISTRY

PAPER

View Article Online
View Journal | View Issue

Check for updates

Cite this: J. Mater. Chem. A, 2026, 14, 4226

Towards mitigating ring opening in TEMPO catholytes for aqueous redox flow batteries

Diqing Yue,[a] Sepideh Biabanialitappeh,[a] Mahla Sarfaraz Khabbaz,[a] Mark D. Woollam,[b] Lifan Zeng,[c] Kee Sung Han,[d] Eric Walter,[d] Peter S. Rice,[d] Vijay Murugesan,[d] Mangilal Agarwal,[b] Aaron Hollas,[e] Wei Wang[e] and Xiaoliang Wei*[a]

TEMPO has been widely explored as one of the most promising catholyte redox scaffolds in aqueous redox flow batteries, but the often-observed performance degradation raises concern with respect to its chemical instability. In this work, we demonstrate that the charged TEMPO species (*i.e.*, $TEMPO^+$) lack sufficient stability and also determine the major decomposition pathways. The decay products of $TEMPO^+$ are experimentally analyzed using combined tools including nuclear magnetic resonance and mass spectroscopy. Reductive conversion to 2,2,6,6-tetramethylpiperidine (TEMPH) is commonly observed for a variety of 4-O-substituted TEMPO derivatives. The general detection of alkene and related carbonyl signals, in conjunction with the electrolyte acidification, reveals a deprotonation-initiated ring opening route that proceeds towards TEMPO decay. The protons on the β carbon are susceptible to chemical extraction by nucleophilic agents such as hydroxyl and the formed piperidine. This finding highlights the intrinsic structural factors for TEMPO degradation and will shed light on the potential stabilization strategies to afford long-cycling TEMPO-based flow batteries.

Received 21st August 2025
Accepted 9th December 2025

DOI: 10.1039/d5ta06814b

rsc.li/materials-a

Open Access Article. Published on 09 December 2025. Downloaded on 4/6/2026 10:10:55 PM. This article is licensed under a Creative Commons Attribution 3.0 Unported Licence.

1. Introduction

Scalable, cost-effective stationary energy storage solutions are considered effective in accommodating the more dynamic power grid with improved reliability, resiliency, and affordability. Redox flow batteries (RFBs) are highly competitive storage technologies because of their capability of tolerating different grid applications with diversified energy to power (E/P) ratios.[1–3] This advantage stems from the spatially decoupled energy and power in RFBs that leads to superior scalability and design flexibility. The electro-active materials (or redoxmers) are the central component of RFB systems and are dissolved as the anolyte at the negative side and as the catholyte at the positive side, respectively. Traditional metal redoxmer-based RFBs have encountered key challenges such as high chemical cost, limited material choices, low solubility and energy density, and/or environmental unfriendliness.[4–7] Organic redoxmers are promising alternatives that can overcome these drawbacks because of their structural diversity, molecular tailorability, wide redox potential distribution, and natural abundance.[8–13] Various organic redoxmers have demonstrated encouraging performance in RFBs. A majority of these redoxmers are used as anolyte materials such as anthraquinone,[14,15] phenazine,[16,17] viologen,[18,19] alloxazine,[20,21] fluorenone,[22] *etc.* However, organic catholyte redoxmers are relatively under-developed and only a few types of redox scaffolds have been deeply studied such as ferrocene and 2,2,6,6-tetramethyl-1-piperidinyloxy (TEMPO).[23–26] Limited long-term stability is one of the most critical challenges for organic catholyte redoxmers especially for those having high redox potentials. Typically, a water molecule bears an electron lone pair, making it possible to nucleophilically attack the cationic moieties of catholyte redoxmers especially in the charged state.[27,28] Other non-water-involving decomposition mechanisms have also been reported for organic catholyte redoxmers. For instance, phenoxazine-based molecules can undergo parasitic halogenation reactions that form non-soluble side products and result in capacity fading.[29] Understanding the origins of structural degradation is of fundamental importance for guided design of stable redoxmers through blocking the confirmed degradation pathways.

Among the various organic catholytes, TEMPO derivatives have been widely investigated. TEMPO bears a sterically protected, stable nitroxide radical as the redox center. Because of its exceptionally high solubility in organic solvents, TEMPO has been investigated as a catholyte redoxmer in nonaqueous RFBs.[30–32] Structural incorporation with hydrophilic substituents is required for TEMPO to afford good solubility for use in aqueous

[a]School of Mechanical Engineering, Purdue University, 723 West Michigan Street, Indianapolis, IN, 46202, USA. E-mail: wei304@purdue.edu
[b]Integrated Nanosystems Development Institute, Indiana University Indianapolis, 625 West Michigan Street, Indianapolis, IN, 46202, USA
[c]Chemical Genomics Core, School of Medicine, Indiana University, Indianapolis, IN 46202, USA
[d]Physical and Computational Sciences Directorate, Pacific Northwest National Laboratory, 3340 Stevens Drive, Richland, WA 99354, USA
[e]Energy and Environment Directorate, Pacific Northwest National Laboratory, 3340 Stevens Drive, Richland, WA 99354, USA

This journal is © The Royal Society of Chemistry 2026

Open Access Article. Published on 09 December 2025. Downloaded on 4/6/2026 10:10:55 PM.
This article is licensed under a Creative Commons Attribution 3.0 Unported Licence.

RFBs.[26,33–35] In an earlier effort, we demonstrated that 4-hydroxy-TEMPO (TEMPOL) served as a highly soluble catholyte redoxmer and was coupled with methyl viologen (MV^{2+}) anolyte in an aqueous RFB chemistry (Fig. 1a).[18] Also shown are the electrochemical reactions of both redoxmers (Fig. 1b). Upon charging, MV^{2+} receives an electron and produces its radical cation form $MV^{+\bullet}$, while TEMPOL loses an electron yielding an oxoammonium form (*i.e.*, $TEMPOL^{+}$). Despite the advantages of high solubility (>2 M) and low cost, the cycling stability of this system remains a concern because capacity fading has been observed at high redoxmer concentrations. As shown in Fig. 1c, the 0.5 M TEMPOL/MV^{2+} flow cell demonstrates an average coulombic efficiency (CE) of 98.1% and rapid capacity decay losing 70% of its initial capacity after 155 cycles (corresponding to 77 h). A low current density of 10 mA cm^{-2} was used to better observe performance degradation through maintaining the redoxmers in the charged states for relatively long periods of time. Surprisingly, both electrolytes became rather acidic over the cycling. pH values of the anolyte and the catholyte dropped from 6.27 to 2.77 and from 9.60 to 0.37, respectively (Fig. 1d). The drawback of fast cycling degradation will greatly limit this system in practical grid applications.

Here, we revisit the TEMPOL/MV^{2+} RFB system through probing the potential degradation mechanisms and developing the chemically stabilized redoxmers. Combined electrochemical, spectroscopic, and computational characterization studies have been carried out to diagnose the structural evolutions of redox molecules. The analysis results indicate that the TEMPOL catholyte is the main performance limiting side. The charged TEMPOL scaffold is highly susceptible to a variety of co-existing decomposition pathways including oxidation and ring-opening reactions. Inspired by the fundamental structure–stability interplay, a series of TEMPO derivatives are designed so that the decomposition factors are mitigated to produce improved chemical stability and cycle life.

2. Experimental

2.1 Materials and methods

2.1.1. Materials. Methyl viologen (MV^{2+}) dichloride hydrate (98%), 4-hydroxy-TEMPO (TEMPOL, 97%), sodium chloride (NaCl, ≥99.5%), iron(II) chloride tetrahydrate ($FeCl_2 \cdot 4H_2O$, ≥99.0%), sodium hydroxide (NaOH, ≥97.0%), potassium chloride (KCl, ≥99.0%), and D_2O (99.9%) were purchased from Sigma-Aldrich. Sodium hydride (NaH, 60% dispersion in mineral oil), 1,3-propanesultone (≥99%), chloroacetyl chloride (98%), trimethylamine (2 M in tetrahydrofuran), sodium bicarbonate ($NaHCO_3$, 99.5%), magnesium sulfate ($MgSO_4$, anhydrous, 99.5% min), hydrochloric acid (HCl, 37%), pyridine (anhydrous, 99.5+%), toluene (99.85%, Extra Dry), dichloromethane (CH_2Cl_2, 99.7+%), methanol (MeOH, >99.8%), *N*,*N*-dimethylformamide (DMF, 99.8%, Extra Dry), and tetrahydrofuran (THF, 99.5%, Extra Dry) were purchased from Fisher. SELEMION® AMV membranes were purchased from AGC Engineering (Japan) and Nafion® 212 membranes were purchased from Ion Power (Tyrone, PA). All membranes were soaked in deionized water before use. SIGRACELL® graphite felts (GFD, 3 mm thick) were obtained from SGL Carbon (Germany). Deionized water was purged with N_2 overnight before use for preparing the electrolytes. Until otherwise specified, all electrochemical experiments including cyclic voltammetry (CV) and flow cell tests were carried out in a N_2-filled Vigor© SG2400/750 TS glove box with H_2O and O_2 levels less than 1 ppm (Houston, TX).

2.2 Synthesis of redox molecules

The synthetic procedures and spectral characterization of various redox molecules used in this study are described in detail in Supplementary Section S1 and Fig. S1–S7. The synthetic molecules included sodium 4-(1′-propoxy-3′-

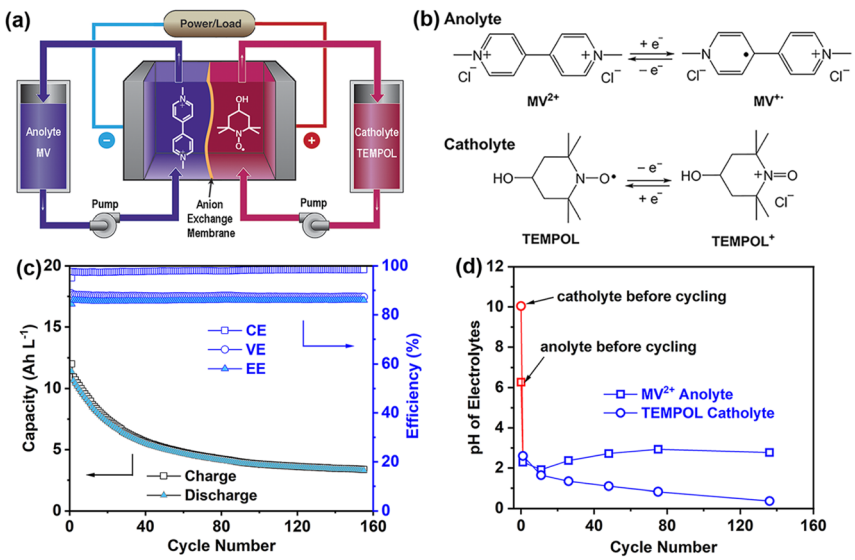

Fig. 1 The TEMPOL/MV^{2+} RFB system: (a) a schematic illustration; (b) electrochemical reactions of both redoxmers; (c) cycling efficiencies and capacities with 0.5 M redoxmers at 10 mA cm^{-2}; (d) pH values of the anolyte and catholyte over the cycling in Panel (c).

Open Access Article. Published on 09 December 2025. Downloaded on 4/6/2026 10:10:55 PM. This article is licensed under a Creative Commons Attribution 3.0 Unported Licence.

sulfonate)-TEMPO (SPrO-TEMPO), (4′-TEMPO) 2-(trimethylammonium chloride)acetate (TMA-Ac-TEMPO), *N*,*N*′-bis(3-sulfonyl-1-propyl)viologen (SPr-V), and *N*,*N*′-bis(3-trimethylammonium-1-propyl)viologen (NPr-V). ^{1}H and ^{13}C nuclear magnetic resonance (NMR) spectra of these synthetic compounds were collected using a Bruker UltraShield 500 MHz spectrometer.

2.3 CV tests

CV experiments were performed using a CHI660D potentiostat (CH Instruments) with a three-electrode cell including a glassy carbon working electrode (3 mm diameter), Ag/AgCl reference electrode (saturated KCl), and a graphite felt strip counter electrode. The electrolyte contained 10 mM redox molecules in 0.5 M NaCl. The voltammograms were collected at the scan rate υ varying from 0.01 to 0.5 V s^{-1} to determine the diffusion coefficient (D) using the Randles-Sevcik eqn (1):[36]

$$i_p = 0.4463(nF)^{3/2}AC(\upsilon D/RT)^{1/2} \quad (1)$$

where i_p is the peak current, n is the number of electrons, F is the Faraday constant (96 485 C mol^{-1}), A is the electrode area (0.071 cm^2), C is the redoxmer concentration (10 mM), T is the temperature (298 K), and R is the gas constant (8.314 J K^{-1} mol^{-1}). The diffusion coefficients in the charging and discharging processes (D_O and D_R) were estimated from the slopes of the respective linear i_p *vs.* $\upsilon^{1/2}$ plots. D was obtained as the average of D_O and D_R.

The electron transfer rate constant (k_0) was estimated using the Nicholson's method from eqn (2) and (3):[36]

$$\Psi = (-0.6288 + 0.0021\Delta E_p)/(1 - 0.017\Delta E_p) \quad (2)$$

$$\Psi = k_0(\pi DnF/RT)^{-1/2}\upsilon^{-1/2} \quad (3)$$

where Ψ is the kinetic parameter and ΔE_p is the peak separation in the voltammogram. k_0 was calculated from the slope of the linear Ψ *vs.* $\upsilon^{-1/2}$ plot.

2.4 Flow cell tests

The flow cells were assembled with thermally treated GFD electrodes sandwiching an ion exchange membrane with an active area of 20 cm^2. For cationic redoxmers, SELEMION® AMV anion exchange membranes were used. For anionic redoxmers, Nafion® 212 cation exchange membranes were used and were converted to the Na^+ form by soaking in 1 M NaOH for 24 h. The electrolytes were 10 mL of 0.5 M redoxmers in 1.5 M supporting NaCl. A Masterflex® L/S® peristaltic pump (Cole-Parmer) was used to circulate the electrolytes through the cell compartment at a flow rate of 20 mL min^{-1}. Galvanostatic cycling was performed at a current density of 10 mA cm^{-2} using Arbin BT-2000 (Arbin Instruments, College Station, TX) or Neware CT-4008-5V6A (Neware, China) battery testers with specified voltage cutoffs.

If necessary, the pH values of the anolyte and catholyte were measured in the discharged states at specified cycles using an Accumet™ Excel XL 15 pH meter. The cycled anolyte and catholyte of selected flow cells were sealed with CRITOSEAL® and characterized by NMR. For flow cells that needed post-cycling analysis, D_2O was used as the solvent (instead of H_2O).

2.5 EPR measurements

The $MV^{+\bullet}$ solution was electrochemically prepared by charging up an MV/Fe flow cell that used an anolyte of 0.5 M MV/1.5 M NaCl, a catholyte of 0.6 M $FeCl_2$/1.5 M NaCl, and an AMV membrane inside a N_2-filled PLAS-LABS 830-ABD purge box (LANSING, MI). This flow cell was charged at 25 mA cm^{-2} then at 10 mA cm^{-2} and then at 5 mA cm^{-2} in the N_2 glove box until the voltage reached 1.35 V. A small portion (~50 μL) of the charged $MV^{+\bullet}$ sample was double-sealed with CRITOSEAL® in a Teflon tubing (outer and inner diameters of 1/16″ and 1/32″, respectively) then in a 4-mm quartz EPR tube (Wilmad-LabGlass, USA) to avoid exposure to oxygen. The EPR spectra were collected at room temperature as a function of time using a Bruker Elexsys 580 spectrometer fitted with an SHQE resonator with microwave frequency ~9.85 GHz (X band) at 20 mW power.

2.6 NMR measurements

The $TEMPOL^+$ solution was electrochemically prepared by charging up an Fe/TEMPOL flow cell that used an anolyte of 0.6 M $FeCl_2$/1.5 M NaCl, a catholyte of 0.5 M TEMPOL/1.5 M NaCl, and an AMV membrane. Instead of H_2O, D_2O was used as the solvent. This flow cell was charged at 20 mA cm^{-2} then at 10 mA cm^{-2} and then at 5 mA cm^{-2} until the cell voltage reached 1.6 V. The $TEMPOL^+$ sample was sealed with a CRITOSEAL® tube sealant and subjected to temporal NMR measurements.

2.7 Density functional theory (DFT) calculation

DFT calculation of the optimized geometry of $MV^{+\bullet}$ was performed at hybrid functional with Grimme dispersion corrections (B3LYP-D3) and an all-electron triple-zeta double polarization function basis set (TZ2P) inbuilt of ADF2017 software package.[37]

2.8. Gas chromatography-mass spectroscopy (GC-MS)

An $SPrO\text{-}TEMPO^+$ solution was electrochemically prepared by charging up a flow cell using 0.5 M SPrO-TEMPO catholyte (12 mL), 0.5 M SPr-V anolyte (13 mL), and a Na^+ form Nafion 212 membrane. 1.5 M NaCl was used as the supporting electrolyte in both the anolyte and catholyte. The $SPrO\text{-}TEMPO^+$ solution was divided into 3 mL aliquots per sample which were well sealed in Restek headspace vials (Bellefonte, PA). GC-MS analysis was carried out on the $SPrO\text{-}TEMPO^+$ samples with different aging times using an Agilent (Santa Clara, CA) 7890A GC coupled with a 7200 accurate mass quadrupole time-of-flight MS system (GC-MS QTOF) and equipped with an electron ionization (EI) source. If needed, sample heating was performed by maintaining it at 60 °C for 5 min. 1 mL of gaseous headspace was extracted using a Hamilton syringe and was directly injected into the front inlet kept at 250 °C (split ratio 4 : 1 at flow rate = 6 mL min^{-1}). Ultra-high purity helium was used as the carrier gas (flow rate = 1.5

 This journal is © The Royal Society of Chemistry 2026

Open Access Article. Published on 09 December 2025. Downloaded on 4/6/2026 10:10:55 PM. This article is licensed under a Creative Commons Attribution 3.0 Unported Licence.

mL min^{-1}) that ran through a Restek Rxi-5ms column 30 m in length with a 0.25-mm internal diameter and 0.25-μm film thickness. The oven temperature program began with a one-minute hold at 50 °C, followed by a ramp at 50 °C per min until reaching a final temperature of 260 °C (total run time = 5.2 min). Over the course of the run, the mass transfer line was held at 250 °C with the MS operating in full scan mode ranging from 25 to 450 *m*/*z* values (ion source temperature = 250 °C, acquisition rate = 5 spectra per sec). Data were acquired in centroid mode using Agilent MassHunter software, with compound identification and analysis performed through Qualitative Workflows and Navigator using the NIST17 mass spectral library. Ambient air and a 1.5 M NaCl baseline reference were interspersed with the samples of interest to monitor potential carry-over and confirm that detected compounds were not artifacts of the analytical method.

2.9. Liquid chromatography-mass spectroscopy (LC-MS)

LC-MS data were obtained using an Agilent 1290 liquid chromatography (LC) – 6545 quadrupole time-of-flight (QTOF) spectrometer with direct injection or after passing through an Agilent ZORBAX 300SB-C3 column (4.6 × 50 mm 3.5-micron). Water and MeCN mixtures in a gradient containing 0.1 vol% formic acid were used as the mobile phase to facilitate molecule separation in the column.

3. Results and discussion

3.1 Degradation mechanism analyses

MV^{2+} in the uncharged states is commercially available with a long shelf life and thus is chemically stable. TEMPOL is a commercially available nitroxide free radical and has a year-scale shelf life under the manufacturer's storage conditions (*e.g.*, in a cold and light-free place). In fact, their charged states dictate the cycling stability of TEMPOL/MV^{2+} flow cells. To unravel the possible root causes for the capacity fading shown in Fig. 1, the chemical stabilities of the charged states of both redoxmers were investigated under *ex situ* conditions. The obtained understanding of stability-controlling factors is expected to offer insights on rationalization of potential performance mitigation strategies.

3.1.1 Decomposition reactions of the anolyte. The charged species of MV^{2+}, *i.e.*, the $MV^{+\bullet}$ radical cation, was electrochemically prepared by charging up a 0.5 M MV/$FeCl_2$ flow cell. This setup takes advantage of $Fe^{2+/3+}$ conversion at the catholyte side of this flow cell. According to the voltage curve in Fig. 2a, 82% of its theoretical capacity was charged, corresponding to an $MV^{+\bullet}$ concentration of 0.41 M. After completion of charging, the pH of the MV anolyte slightly changed from 6.27 to 6.04. The fresh $MV^{+\bullet}$ sample was well sealed to avoid air exposure and was subjected to EPR characterization as a function of standing time. As shown in Fig. 2b, the EPR integral (representing the radical concentration) remains nearly unchanged over a time period of ~20 days, demonstrating the superior chemical stability of $MV^{+\bullet}$ under near-pH-neutral conditions. A similar temporal EPR test with a higher 1.02 M $MV^{+\bullet}$ concentration again results in near-constant EPR integrals throughout 11 days (Fig. 2c and S8). The concentration-independent chemical inertness provides strong evidence to confirm radical persistence. The durability is further supported by DFT calculation (Fig. 2d). The optimized geometry of $MV^{+\bullet}$ adopts a perfectly coplanar conformation leading to a high extent of spin and charge delocalization over both aromatic rings.

The stepwise disproportionation–protonation reactions depicted in Fig. 2e have been widely accepted as the major molecular decomposition mechanisms of $MV^{+\bullet}$ in O_2-free inert environments.[38–41] Two planar $MV^{+\bullet}$ species tend to approach each other in a face-to-face configuration, which can initiate

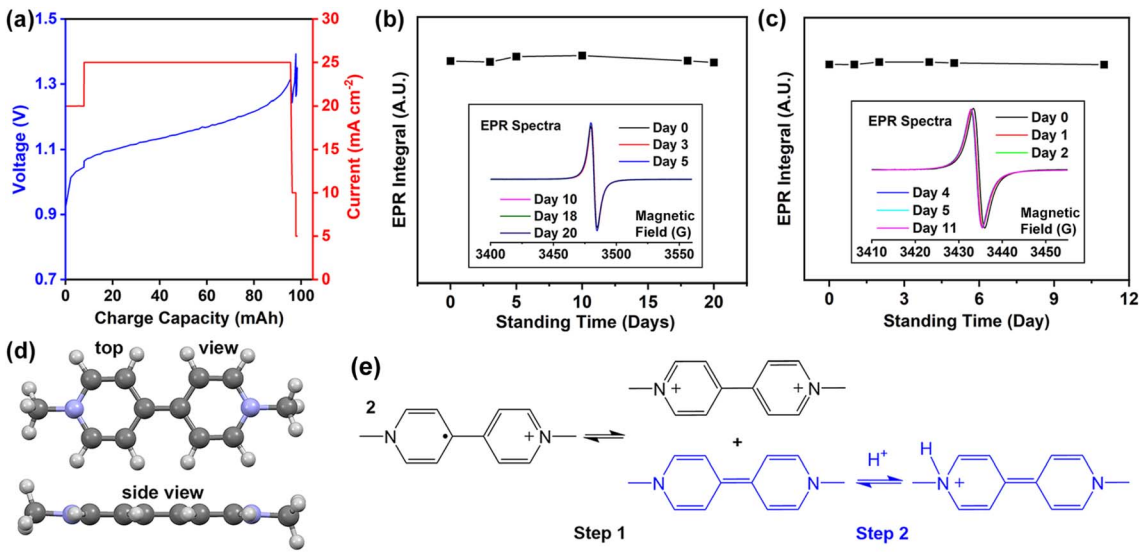

Fig. 2 *Ex situ* stability study of $MV^{+\bullet}$: (a) voltage curve of 0.5 M MV^{2+}/Fe^{2+} flow cell used to prepare 0.41 M $MV^{+\bullet}$ solution ($FeCl_2$ was used in excess); (b) EPR spectra (inset) and integrals of 0.41 M $MV^{+\bullet}$ as a function of standing time; (c) EPR spectra (inset) and integrals of 1.02 M $MV^{+\bullet}$; (d) calculated optimized geometry of $MV^{+\bullet}$; (e) proposed disproportionation and protonation equilibria of $MV^{+\bullet}$.

Open Access Article. Published on 09 December 2025. Downloaded on 4/6/2026 10:10:55 PM. This article is licensed under a Creative Commons Attribution 3.0 Unported Licence.

a disproportionation-based charge transfer reaction proceeding to form the parent MV^{2+} and the double-reduced MV^{0}. Protonation of MV^{0} generates a redox-inactive H-adduct. Under pH-neutral conditions, which is the case for the above *ex situ* stability test, these two reactions occur in equilibrium, resulting in well-maintained $MV^{+\bullet}$ concentrations in standalone solutions. However, in acidic environments, the higher H^{+} concentration will drive the equilibria to the right side towards formation of the H-adduct, thus causing irreversible loss of the $MV^{+\bullet}$ radical (Fig. S9). In the 0.5 M TEMPOL/MV^{2+} flow cell (Fig. 1), the pH value of the MV^{2+} anolyte dropped to ~2 during the cycling, in which $MV^{+\bullet}$ became unstable. The stark contrast between the standalone and the operational $MV^{+\bullet}$ electrolytes suggests that the MV^{2+} anolyte is not responsible for the undesired generation of protons. Therefore, we shifted our focus to the catholyte side.

3.1.2 Decomposition reactions of the catholyte. The charged oxoammonium form of TEMPOL, *i.e.*, $TEMPOL^{+}$, was electrochemically prepared by charging up a 0.5 M $FeCl_2$/TEMPOL flow cell, in which the $Fe^{0/2+}$ redox couple was used as the anolyte. D_2O was used as the solvent in this flow cell to facilitate NMR testing and reduce water background signal. According to the voltage profile shown in Fig. S10, 96% of TEMPOL was converted yielding 0.48 M $TEMPOL^{+}$. After completion of charging, the pH of the TEMPOL electrolyte was changed from 10.04 to 1.21, corresponding to a fairly acidic $TEMPOL^{+}$ solution. As the $Fe^{0/2+}$ redox reaction does not involve protons, such an abrupt pH drop in $TEMPOL^{+}$ electrolyte suggests that $TEMPOL^{+}$ may be the source of proton generation in TEMPOL/MV^{2+} flow cells. Moreover, the low pH is not healthy for the nitroxide radical in TEMPOL. As shown in Fig. 3a, TEMPOL is susceptible to decomposition *via* a disproportionation pathway forming $TEMPOL^{+}$ and redox-inactive hydroxylamino (4-HO-TEMPOH) or its N-protonated form.[42–44] Interestingly, the TEMPOL radical remains stable when the pH value is 2.4 or above, but an EPR signal decay occurs at pH 0 (Fig. 3b).

To elucidate the pathways of proton generation from $TEMPOL^{+}$, the freshly prepared $TEMPOL^{+}$ solution was analyzed using temporal ^{13}C NMR thanks to its diamagnetic nature. The result is plotted in Fig. 3c. NMR signal was not detected in freshly prepared $TEMPOL^{+}$ due to fast exchange with the residual TEMPOL radicals in the sample. After ~12 h, the sample became NMR-sensitive and the signal grew stronger with time, indicating a gradual formation of diamagnetic molecules. Most importantly, carbon peaks atypical to the TEMPOL structure emerged, indicating occurrence of drastic structural changes. For example, the peaks within the 200–220 ppm range are characteristic of carbonyl (C═O) bonds (highlighted in the green box), and those at 130–150 ppm typically belong to unsaturated alkene C═C bonds (highlighted in the blue box). Similar ^{13}C NMR peak patterns were obtained from a $TEMPOL^{+}$ sample prepared differently *via* charging up a 0.5 M TEMPOL/MV^{2+} flow cell (Fig. S11). These new peaks, which cooperate with the substantial pH drop, provide important clues on the nature of decomposition reactions of $TEMPOL^{+}$.

The charged form of nitroxide radical, *i.e.*, oxoammonium ($^{+}N{=}O$), is an oxidant and has been used to convert alcohols to aldehydes or ketones in organic synthesis.[45] Because of the presence of a hydroxyl group (–OH) in TEMPOL or $TEMPOL^{+}$, we hypothesize that the oxoammonium moiety ($^{+}N{=}O$) oxidizes the –OH groups following the conversion mechanism depicted in Fig. 3d. This side reaction yields ketone structures, which explains the appearance of carbonyl peaks in ^{13}C NMR. This process involves release of a free proton (H_3O^{+}), which agrees with the pH drop and further validates our hypothesis. In TEMPOL/MV^{2+} flow cells, the protons generated in the catholyte

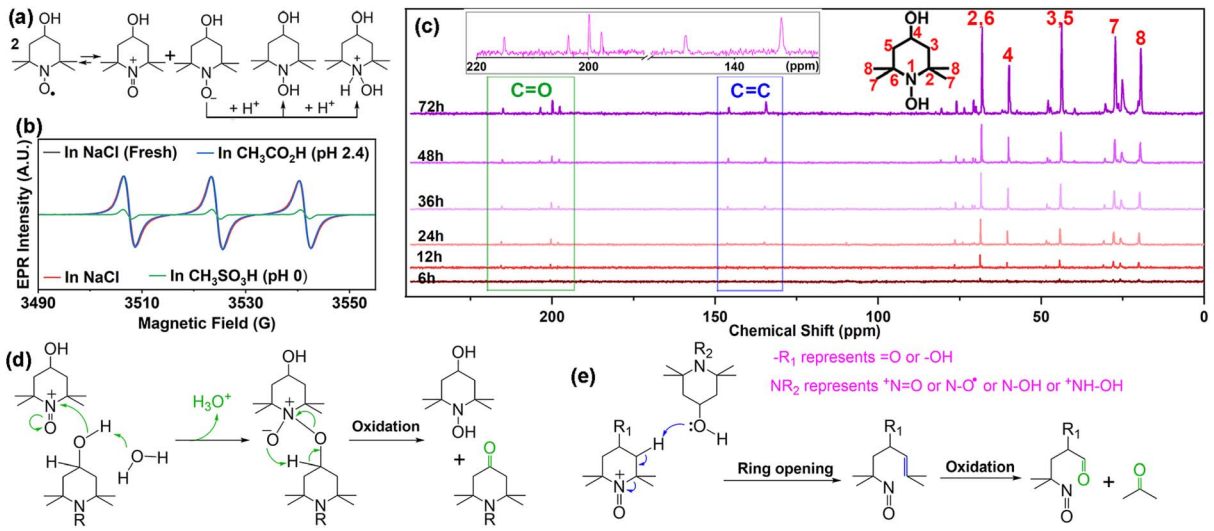

Fig. 3 *Ex situ* study of the chemical stability of $TEMPOL^{+}$: (a) proposed acid-catalyzed disproportionation of TEMPOL; (b) EPR spectra of 10 mM TEMPOL radical at different pH values taken 24 hours after preparation; (c) temporal ^{13}C NMR of electrochemically prepared $TEMPOL^{+}$ (inset) an expanded view of the 72 h spectrum; the structure of 4-hydroxy-TEMPOH); (d) proposed alcohol oxidation reaction, and (e) proposed ring-opening side reaction and following oxidative cleavage of the C═C bond.

 This journal is © The Royal Society of Chemistry 2026

Open Access Article. Published on 09 December 2025. Downloaded on 4/6/2026 10:10:55 PM.
This article is licensed under a Creative Commons Attribution 3.0 Unported Licence.

will permeate through the membrane to the anolyte and de-energize the $MV^{+\bullet}$ redox (Fig. 2e), causing loss of both redoxmers.

According to the prior ^{13}C NMR studies of $TEMPO^+$,[46,47] the carbon atoms at 2,6-sites (*i.e.*, C(2,6)) in $TEMPOL^+$ are expected to have a chemical shift at around 100–105 ppm, but this characteristic peak is not visible in Fig. 3c. This is presumably because of the rapid chemical exchange between the diamagnetic $TEMPOL^+$ cation and the paramagnetic TEMPOL radical, which suppresses the NMR response of the carbon atoms adjacent to $^+N{=}O$.[48] We speculate that the major peaks at 68, 60, 44, 27, and 19 in Fig. 3c belong to the C(2,6), C(4), C(3,5), C(7), and C(8), respectively, of 4-HO-TEMPOH (Fig. 3c inset) or its N-protonated form. Such peak assignments are supported by the proton-coupled ^{13}C NMR shown in Fig. S12 and a prior ^{13}C NMR study of TEMPOH.[49] The potential sources of 4-HO-TEMPOH include the co-product of alcohol oxidation (Fig. 3d) and the disproportionation product of TEMPOL under acidic pH (Fig. 3a). Besides these major peaks, the many weaker aliphatic carbon peaks below 80 ppm suggest the presence of multiple species that originated from $TEMPOL^+$, which could be explained by the multiple possibilities indicated in Fig. 3d (the magenta note).

The appearance of C=C peaks in ^{13}C NMR of the aged $TEMPOL^+$ solution indicates occurrence of additional decomposition routes. Parasitic ring-opening reactions have been previously suggested for TEMPO-based redoxmers in the charged states.[34,44,50,51] We apply this mechanism to $TEMPOL^+$ degradation following the pathway schemed in Fig. 3e. The –OH group in TEMPOL or $TEMPOL^+$ deprotonates the β-position carbon leading to elimination reactions that form alkene moieties in the structure. Further deprotonation at the other β-carbon may occur producing a diene structure. The C=C bonds are unstable and can be irreversibly oxidized either chemically by the oxoammonium ($^+N{=}O$) oxidant or electrochemically by the electric field. The oxidative cleavage of the trisubstituted C=C bonds can produce ketone and aldehyde molecules. To test this possibility, headspace GC-MS measurement was carried out on such a $TEMPOL^+$ sample and the presence of volatile acetone was detected (Fig. S13). The GC-MS result validates the proposed ring opening-based alkene formation, which also explains an additional origin of C=O generation.

To further confirm the decomposition mechanisms and identify additional side products, high-resolution LC-MS analysis was performed to a $TEMPOL^+$ sample that was aged for 4 days after its electrochemical preparation in a 0.5 M TEMPOL/MV^{2+} flow cell. The result is plotted in Fig. S14. The *m*/*z* values of 4-oxo-TEMPO and protonated 4-HO-TEMPOH were identified, in good agreement with the above ^{13}C NMR finding of parasitic reactions of alcohol oxidation and H^+-catalyzed disproportionation of nitroxide radical. Ring-opening products were not detected in LC-MS, presumably due to their UV-insensitivity. Interestingly, the deoxygenated species, 4-hydroxy-2,2,6,6-tetramethylpiperidine (4-HO-TEMPH) and its protonated form, were also detected. Such TEMPH-based conversion products have been previously reported for TEMPO derivatives, with or without the 4-O-substituents, in the context of aqueous RFBs[52,53] and chemical syntheses.[54–56] It was mentioned that TEMPOH was unstable, which was converted to TEMPO under aerobic conditions and spontaneously disproportionated into TEMPO and TEMPH in an inert atmosphere.[56] However, the detailed conversion mechanism is not well understood. Here we propose a disproportionation-based reaction route involving a homolysis process, which is depicted in Fig. S15. Validation of this pathway requires substantial further evidence, which is not in the scope of the current study.

3.1.3 Crossover loss of redoxmers. Through-membrane crossover of redoxmers is considered as a common source of capacity fading in RFBs. To investigate this possibility, the cycled anolyte and catholyte were analyzed using NMR measurements. Fig. 4 plots the ^1H and ^{13}C NMR spectra of the anolyte and the catholyte before and after cycling of a 0.5 M TEMPOL/MV^{2+} flow cell. In the ^{13}C NMR (Fig. 4a), the MV^{2+} structure only has one aliphatic resonance at 43 ppm that

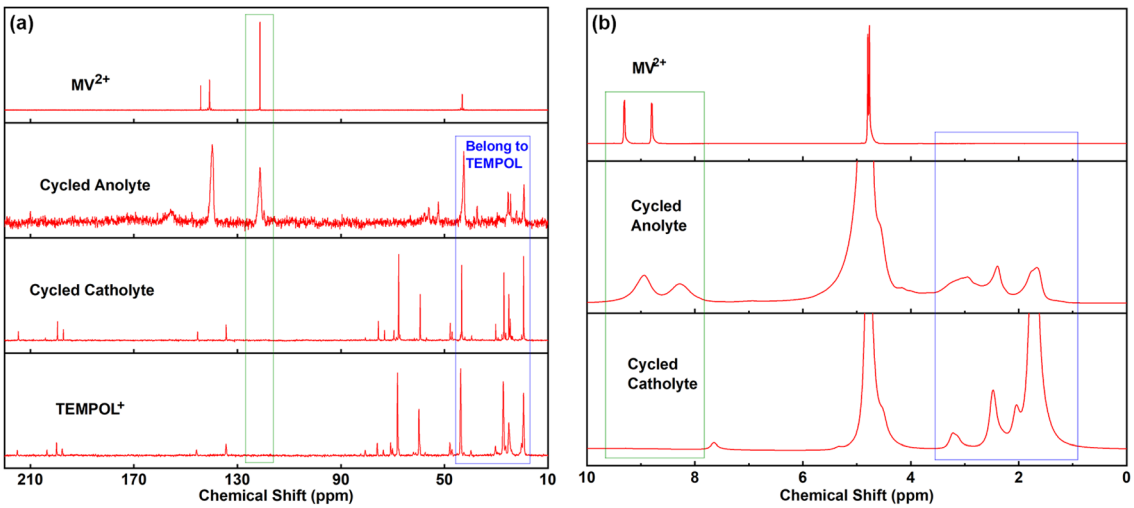

Fig. 4 (a) ^{13}C NMR and (b) ^1H NMR of the anolyte and the catholyte before and after cycling of a 0.5 M TEMPOL/MV^{2+} flow cell.

Open Access Article. Published on 09 December 2025. Downloaded on 4/6/2026 10:10:55 PM. This article is licensed under a Creative Commons Attribution 3.0 Unported Licence.

belongs to the methyl groups. But the cycled anolyte contains complicated aliphatic peaks in the range of 0–90 ppm (highlighted by the blue box). Because of the diffused distribution, it is reasonable to assume these peaks unlikely correspond to MV^{2+}-derived species. Instead, such a peak pattern more resembles that of the $TEMPOL^{+}$-based molecules. Similarly, $TEMPOL^{+}$-related aliphatic proton peaks are detected in the ^{1}H NMR of the cycled anolyte within a range of 1–4 ppm (highlighted by the blue box in Fig. 4b). No ^{1}H or ^{13}C NMR peaks of MV^{2+} show up in the corresponding regions of the cycled catholyte (green boxes in both panels of Fig. 4). The NMR results suggest that crossover of TEMPOL species occurred during battery cycling. TEMPOL is a neutral molecule and its permeation through an ion exchange membrane is possible. This result agrees well with the detection of TEMPOL crossover through anion exchange membranes in a previous study.[26]

With a similar analysis, crossover of MV^{2+} species from the anolyte to the catholyte was not obvious. The cycled catholyte exhibits a ^{13}C NMR pattern near-identical to $TEMPOL^{+}$, with the presence of carbonyl (C═O) and alkene peaks. No characteristic aromatic carbon peaks of MV^{2+} are observed. On the one side, $TEMPOL^{+}$ in the flow cell follows a similar decomposition pathway to the standalone conditions. On the other hand, we believe that MV^{2+} crossover is minimal, primarily because its highly cationic structure encounters strong Donnan exclusion effects that prevent its permeation. This argument is further supported by the ^{1}H NMR (Fig. 4b). The characteristic aromatic proton peaks of MV^{2+} are not seen between 8 and 10 ppm in the cycled catholyte.

Based on the above decomposition product and crossover analyses, we can safely reach a conclusion that TEMPOL catholyte is the major limiting side for the TEMPOL/MV^{2+} RFB system. The –OH group triggers molecular decomposition of $TEMPOL^{+}$ mainly including oxidation and ring-opening reactions. The substantial pH drop causes the disproportionation of TEMPOL and the protonation of MV^{0}, resulting in the formation of redox-inactive species. The neutral structure of TEMPOL is unable to resist permeation through an anion exchange membrane. These factors have led to irreversible catholyte redoxmer loss and shortened cycle life. Therefore, a plausible molecular design principle for achieving stable TEMPO candidates is to highlight a hydroxyl-free, ionic structure feature to eliminate these degradation factors.

3.2 Stabilization of TEMPO structures

3.2.1 Anion-bearing TEMPO. Based on the above rationale, our initial effort was to meet the design requirement by devising a hydroxyl-free TEMPO derivative, namely sodium 4-(1′-propoxy-3′-sulfonate)-TEMPO (SPrO-TEMPO). This molecule bears an anionic sulfonate group to enable strong Donnan repulsion with sodiated Nafion 212 and thus is expected to mitigate redox

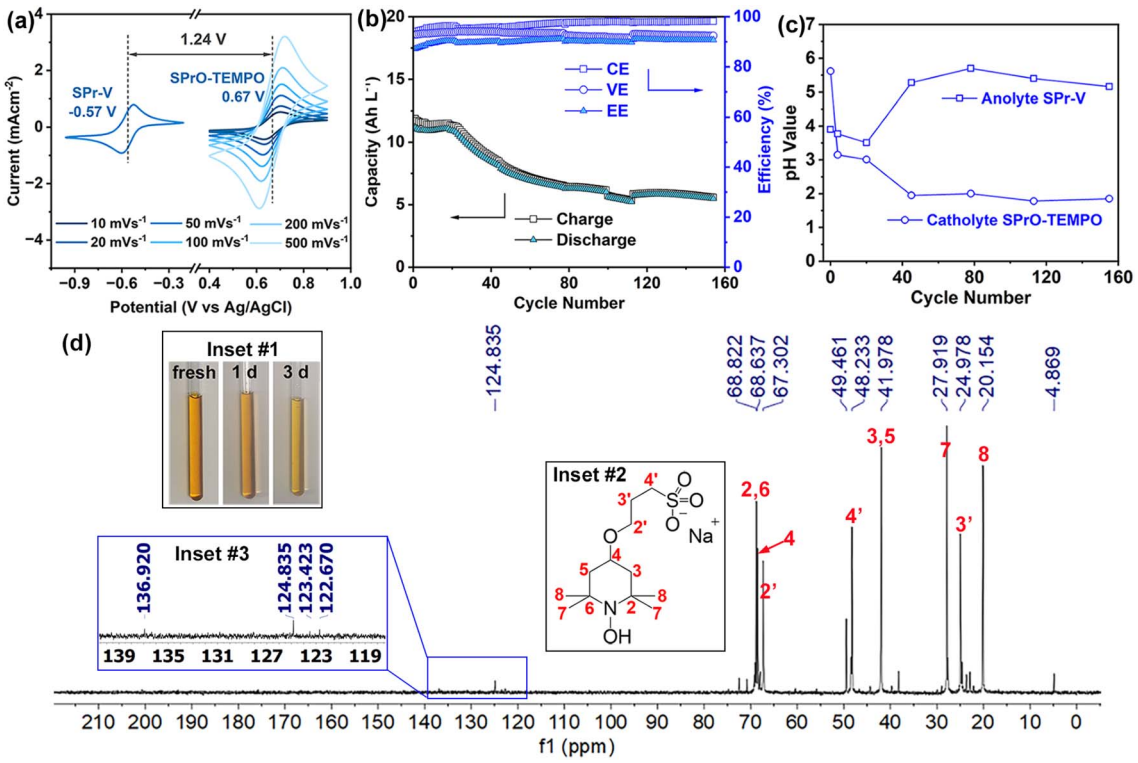

Fig. 5 Stability testing for SPrO-TEMPO: (a) CV scans of 10 mM SPrO-TEMPO and 10 mM SPr-V, respectively, both in 0.5 M NaCl; (b) cycling efficiencies and capacities of a 0.5 M SPrO-TEMPO/SPr-V flow cell at 10 mA·cm^{-2}; (c) pH values of the anolyte and catholyte over the cycling in panel (b). (d) ^{13}C NMR of the charged 0.5 M SPrO-TEMPO^{+} after 3 days of aging. (Inset #1) The gradual color fading of the NMR solution; (inset #2) the assignments of major carbon peaks, which were facilitated by the 2D ^{1}H–^{13}C correlation spectroscopy as shown in Fig. S19; (inset #3) an expanded view of the alkene region.

 This journal is © The Royal Society of Chemistry 2026

Open Access Article. Published on 09 December 2025. Downloaded on 4/6/2026 10:10:55 PM. This article is licensed under a Creative Commons Attribution 3.0 Unported Licence.

material crossover. It was synthesized *via* a one-step reaction between TEMPOL and 1,3-propanesultone in the presence of sodium hydride (NaH) and purified using column chromatography. This TEMPO derivative inherits an aqueous solubility of 2.42 M, a redox potential of 0.67 V *vs.* Ag/AgCl, and an electrochemical kinetic constant (k_0) of 3.68×10^{-3} cm s^{-1} (Fig. 5a and S16). An established stable organic anolyte molecule, *N*,*N*′-bis(3-sulfonylpropyl)-viologen (SPr-V),[57] was used to couple with SPrO-TEMPO to form a new RFB system, leading to a cell voltage of 1.24 V.

To examine the stability of SPrO-TEMPO, a 0.5 M SPrO-TEMPO/SPr-V flow cell was tested under similar conditions to the MV/TEMPOL cell except using a cation exchange membrane (Nafion 212). The cycling capacities and efficiencies are plotted in Fig. 5b. The per cycle time durations of the first 20 stable cycles are ~1.5 h. Surprisingly, despite the high cell efficiencies, rapid capacity fading was still observed, with a 50% loss of the initial capacity after 155 cycles (totally 118 h). The pH value of the SPr-V anolyte was maintained below 4 and was then increased to 5–6 (Fig. 5c). However, the cycled catholyte became fairly acidic and exhibited pH values of ~2 in most of these cycles. Although this is less severe than the parent TEMPOL, the substantial pH drop suggests that SPrO-TEMPO may be subjected to free proton generation. Post-mortem NMR analysis unravels two potential capacity degradation mechanisms. First is the crossover of SPr-V. The ^{1}H NMR of the cycled SPrO-TEMPO catholyte (Fig. S17a) reveals the presence of aromatic ring protons at a range of 9–10 ppm and the pattern resembles that of *N*,*N*′-disubstituted viologen. Because SPrO-TEMPO contains no aromatic structure, we suspect SPr-V anolyte species permeated through the Nafion membrane during the cycling. This is likely because, despite having an ionic nature, SPr-V is an electrically neutral molecule on the whole.

The second capacity fading factor is decomposition of the SPrO-TEMPO$^+$. As shown in Fig. S17b, the ^{13}C NMR spectrum of the cycled SPrO-TEMPO contains several resonance peaks that are characteristic of alkene (C=C) groups in the range of 125–155 ppm. This result echoes with the previous ^{13}C NMR of TEMPOL$^+$ in Fig. 3 indicating the occurrence of alkene formation in the SPrO-TEMPO catholyte. Oxidative cleavage of the formed C=C bonds produced carbonyl (C=O) groups that correspond to the peaks at 216.4 and 176.7 ppm as shown in Fig. S17b. The generated protons from ring opening permeated to the anolyte side shifting the disproportionation equilibria of $MV^{+\bullet}$ towards the redox-inactive H-adduct and thus expedited the performance degradation of the flow cell. To further confirm such a decomposition route of SPrO-TEMPO$^+$, we performed an *ex situ* stability test by observing the NMR spectra of a standalone SPrO-TEMPO$^+$ solution. Fig. 5d shows its ^{13}C NMR plot after three days of aging. The digital photos of the sealed NMR sample (inset #1) display a gradual color fading over time. A few weak alkene (C=C) peaks occur in the range of 120–140 ppm, which agree well with the cycled SPrO-TEMPO$^+$. Among them, the peak at 124.8 ppm is suspected to belong to CO_2, as this chemical shift is close to the reported values for CO_2 in aqueous media.[58–60] This peak assignment was also inspired by a few prior reports of CO_2 formation from structural decay of TEMPO.[44,51] After a 10-day standing time (Fig. S18a), the appearance of more complicated alkene peaks evinces formation of multiple alkene side products. The concurrent carbonyl peak at 176.0 ppm suggests oxidation of unstable C=C bonds. The ^{1}H NMR of this SPrO-TEMPO$^+$ solution in Fig. S18b provides limited direct species identification, but the gradually resolved proton peaks indicate formation of structurally different, diamagnetic molecules.

To cross-validate the decomposition reactions, we performed headspace GC-MS analysis on the aged SPrO-TEMPO$^+$ electrolyte solution. As shown in Fig. S20, a CO_2 signal was clearly identified, together with a handful of volatile alkene products. Interestingly, more types of alkene structures were identified than those in TEMPOL$^+$ electrolytes (Fig. S13). A possible reason is that the –OPrS substituent in SPrO-TEMPO$^+$ is a better leaving group than the –OH group in TEMPOL$^+$, opening the door to additional alkene formation mechanisms such as elimination reactions *via* releasing the $^-$OPrS. CO_2 was produced *via* the ultimate oxidation of unsaturated alkene molecules. These *ex situ* tests corroborate the post-cycling analysis and strongly support the proposed ring opening pathway of SPrO-TEMPO$^+$.

SPrO-TEMPO has been previously reported by another team in a high-power RFB system that delivered superior cycling stability.[52] However, large excess of SPrO-TEMPO was used in their flow cells, which unfortunately blurred the adverse effects of the instability of SPrO-TEMPO$^+$. And TEMPH was indeed detected by LC-MS in their cycled SPrO-TEMPO catholyte. Our chemical analyses offer clear evidence that SPrO-TEMPO still remains as one of the major stability-limiting factors. Based on the combined NMR and GC-MS analyses, we suggest that the decomposition mechanisms of SPrO-TEMPO$^+$ include a mixture of ring-opening and elimination reactions, both of which are initiated by deprotonation, together with ensuing oxidative cleavage of the formed C=C bonds (Fig. S21). Potential proton-extracting nucleophiles in SPrO-TEMPO$^+$ electrolyte may include the anionic sulfonate and the water molecules. Although their high pK_b values ($\geq$14)[61] make them weak proton acceptors, this possibility cannot be easily ignored. Another possible candidate is TEMPH that bears a nucleophilic secondary amino group in its piperidine ring. TEMPH could be formed similarly to that in TEMPOL$^+$ electrolyte (Fig. S15). In this sense, other anionic or even electron-rich functional groups, such as –COO^-, –PO_3^{2-}, –NR_2, –OH, –SH, *etc.*, may similarly trigger the detrimental chemical attacks. Therefore, we should be highly cautious when introducing these nucleophilic substituents into the TEMPO skeleton.

3.2.2 Cationic TEMPO. The above finding shifts our effort to the development of a cationic TEMPO derivative, namely (4′-TEMPO) 2-(trimethylammonium chloride)acetate (TMA-Ac-TEMPO). This molecular design approach resonates with a few prior studies of TEMPO, such as 4-[3-(trimethylammonium)acetylamino]-TEMPO (TMAAcNH-TEMPO)[34] and 4-[3-(trimethylammonio)propoxy]-TEMPO (TMAP-TEMPO)[26] which also bear positively charged substituents. TMA-Ac-TEMPO was successfully synthesized *via* highly scalable two-step reactions: coupling between TEMPOL and chloroacetyl chloride, followed by addition of trimethylamine.

Open Access Article. Published on 09 December 2025. Downloaded on 4/6/2026 10:10:55 PM.
This article is licensed under a Creative Commons Attribution 3.0 Unported Licence.

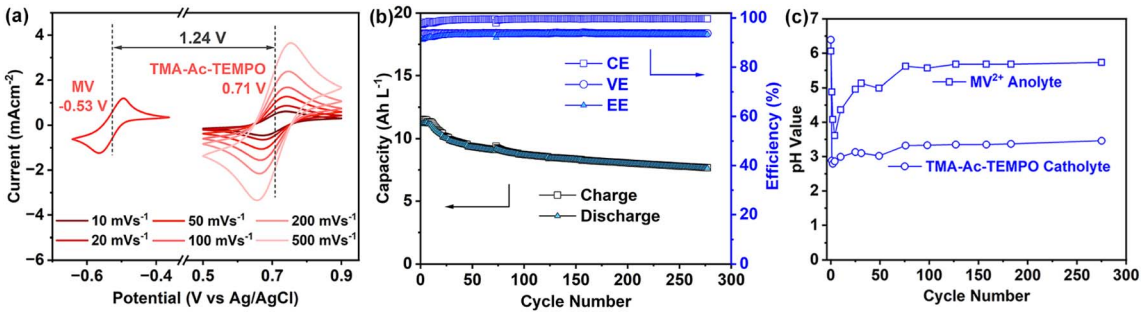

Fig. 6 Stability testing for TMA-Ac-TEMPO: (a) CV scans of 10 mM TMA-Ac-TEMPO and 10 mM MV^{2+}, respectively, both in 0.5 M NaCl; (b) cycling efficiencies and capacities of a 0.5 M TMA-Ac-TEMPO/MV^{2+} flow cell at 10 mA·cm^{-2}; (c) pH values of the anolyte and catholyte over the cycling in panel (b).

The same set of physico-chemical and electrochemical properties were experimentally measured, including an aqueous solubility of 1.81 M, a redox potential of 0.71 V *vs.* Ag/AgCl, and an electrochemical rate constant of 5.96×10^{-3} cm s^{-1} (Fig. 6a and S22). The TMA-Ac-TEMPO catholyte was coupled with the MV^{2+} anolyte with the use of a SELEMION® AMV anion exchange membrane. To evaluate the stability of this new derivative, a TMA-Ac-TEMPO/MV^{2+} flow cell using 0.5 M redoxmers was tested under identical conditions to the TEMPOL/MV^{2+} system shown in Fig. 1c. As shown in Fig. 6b, the flow cell demonstrates an improved cycling stability, losing 32% of its initial capacity after 275 cycles (*i.e.*, 271 h). The acidification of the catholyte turned less serious and the pH value was maintained at ~3, indicating a more than two orders of magnitude lower concentration of produced protons (Fig. 6c). The enhanced cycling performance verifies that the molecular design *via* substituting the hydroxy with a cationic solubilizing group is more favored in mitigating the parasitic reactions of $TEMPO^+$.

However, the capacity fading of this TMA-Ac-TEMPO/MV^{2+} flow cell was fairly high compared to many of the other reported aqueous organic RFB systems.[62] On the one hand, the weakly acidic environment in the anolyte (pH = 3.5–5.5 in Fig. 6c) may make the $MV^{+\bullet}$ radical cation susceptible to the disproportionation-induced activity loss. An alternate viologen structure, namely 1,1′-bis[3-(trimethylammonium)propyl]-4,4′-bipyridinium tetrachloride (NPr-V), has been reported to be more resistive to disproportionation, taking advantage of the bulkier substituents blocking the approaching of two radical cations.[24,63] Using NPr-V instead of MV^{2+} indeed enhanced the cycling stability in flow cells, but the difference in the two capacity fading trends is rather marginal (Fig. S23). It should be noted that capacity fading was also observed by other researchers in similar flow cells that used cationically 4-substituted TEMPO (*i.e.*, TMAAcNH-TEMPO) catholyte and NPr-V anolyte.[34] These results indicate that the viologen anolyte side is not the major stability dictator in flow cells. On the other hand, the TMA-Ac-TEMPO specific factors appear to be the root cause for the performance fading. The *ex situ* ^{13}C NMR test of the charged TMA-Ac-TEMPO$^+$ electrolyte still detected the occurrence of alkene or CO_2 signal, *i.e.*, the 124.9 ppm peak in Fig. S24. The increased peak intensity over time suggests its gradual accumulation in the catholyte. The formation of alkene or CO_2 implies that the deprotonation and ring opening process was not well prevented even with this cationic substituent. Moreover, as shown in Fig. S25, the high-resolution LC-MS spectra reveal the existence of TMA-Ac-TEMPO, TMA-Ac-TEMPOH, and TMA-Ac-TEMPH in an aged TMA-Ac-TEMPO$^+$ electrolyte. The formation of TMA-Ac-TEMPH follows a similar reaction route to 4-HO-TEMPH (Fig. S15). It is likely that the TEMPH served as the nucleophilic deprotonating agent that initiated the ring-opening reaction, although the roles of Cl^- counterion and water remain undetermined in the process. In addition, researchers proposed that water molecules could induce other TEMPO$^+$ failure processes such as hydrolyzation of the oxoammonium group.[50,64]

The detection of TEMPH in the TEMPOL$^+$, SPrO-TEMPO$^+$, TMA-Ac-TEMPO$^+$, other RFB-based TEMPO derivatives,[52,53] and unsubstituted TEMPO$^+$ reported in prior chemical synthesis cases[54–56] suggests that TEMPH formation is a ubiquitous conversion reaction for the TEMPO skeleton. We strongly recommend that such a decomposition pathway be considered as one of the major roadblocks in efforts to design stable TEMPO structures.

Based on our mechanistic analysis, Fig. 7 illustrates the general molecular decomposition reactions of TEMPO redoxmers. We speculate that substituting the protons on β-

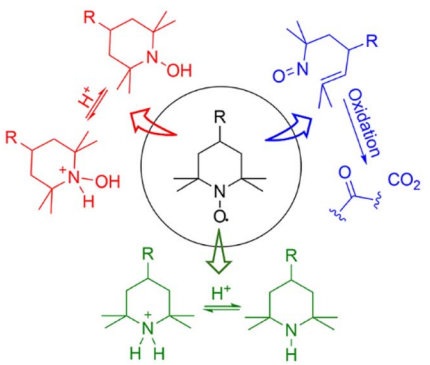

Fig. 7 General decomposition reactions of the TEMPO redox scaffold.

 This journal is © The Royal Society of Chemistry 2026

Open Access Article. Published on 09 December 2025. Downloaded on 4/6/2026 10:10:55 PM. This article is licensed under a Creative Commons Attribution 3.0 Unported Licence.

carbon can block the ring opening route, but the difficulty associated with synthesis of such molecular structures is non-trivial. Currently, a majority of structural engineering strategies lie in tailoring the 4-position functionality. Some of these methods have produced substantial stabilization effects on TEMPO,[34,35,53] but the detailed rationale has yet to be established. Particularly, a recent report indicates that decreasing the Hirshfeld charge of the β-H can intrinsically resist its extraction and lead to enhanced stability for $TEMPO^+$,[50] which may inspire more effective design approaches for achieving stable TEMPO.

4. Conclusions

In conclusion, we have experimentally demonstrated the major decomposition mechanisms of TEMPO-based redoxmers in aqueous RFB environments. From a structural evolution from TEMPOL to 4-O-substituted TEMPO derivatives, they are commonly susceptible to reductive conversion to TEMPH side products. Meanwhile, the protons at the β-positions become vulnerable to chemical extraction by nucleophilic functionalities present in electrolyte solutions such as hydroxyl and piperidine with uncertain possibilities of sulfonate, chloride, or water. Particularly, the role of the piperidinyl amino in TEMPH structures in irreversibly decomposing the TEMPO scaffold has long been under-estimated. The deprotonation-initiated ring opening reactions represent the main decomposition process, which is evidenced by the versatile observation of formation of alkenes and related carbonyl groups in charged TEMPO electrolytes. This mechanism makes it risky to introduce nucleophilic solubilizing substituents into the TEMPO redox scaffold, and even cationically functionalized TEMPO can encounter this decomposition pathway. Even though 4-O-substitution has resulted in improved cycle life in TEMPO-based flow cells, this approach may not be sufficiently effective to achieve stable TEMPO candidates. Fundamentally new structural tailoring methods are in dire need to stabilize the TEMPO redoxmers to a practically relevant time scale. We suggest that more attention be paid to devising molecular strategies that can mechanistically block the pathway for TEMPH formation.

Author contributions

Conceptualization, X. W.; investigation, D. Y., S. B., M. S. B., M. D. W., K. S. H., E. W., P. S. R., V. M., and A. H.; resources, L. Z., V. M., E. W., M. A., W. W., and X. W.; data curation, X. W.; writing – original draft preparation, X. W.; writing – review and editing, L. Z., P. S. R., M. D. W., W. W., and X. W.; visualization, X. W.; supervision, W. W. and X. W.; project administration, W. W. and X. W.; funding acquisition, W. W., V. M., and X. W. All authors have read and agreed to the published version of the manuscript.

Conflicts of interest

There are no conflicts to declare.

Data availability

The data presented in this article are in the format of figures. The data supporting this article have been included as part of the supplementary information (SI). Supplementary information is available. See DOI: https://doi.org/10.1039/d5ta06814b.

Acknowledgements

This work was supported by the U.S. National Science Foundation (Award No. CHE-2055222). The authors at Pacific Northwest National Laboratory (PNNL) would like to acknowledge financial support from the U.S. Department of Energy (DOE) Office of Electricity through its Energy Storage Program under Contract No. 86118. The NMR measurements were performed with a capacity time award (DOI: 10.46936/cpcy.proj.2022.60601/60008671) from the Environmental and Molecular Sciences Laboratory, a DOE User Facility at PNNL. PNNL is operated by Battelle for the U.S. DOE under contract No. DE-AC05-76RLO1830.

Notes and references

1 B. Dunn, H. Kamath and J. M. Tarascon, Electrical Energy Storage for the Grid: A Battery of Choices, *Science*, 2011, **334**(6058), 928–935, DOI: 10.1126/science.1212741.
2 Z. G. Yang, J. L. Zhang, M. C. W. Kintner-Meyer, X. C. Lu, D. W. Choi, J. P. Lemmon and J. Liu, Electrochemical Energy Storage for Green Grid, *Chem. Rev.*, 2011, **111**(5), 3577–3613, DOI: 10.1021/Cr100290v.
3 W. Wang, Q. T. Luo, B. Li, X. L. Wei, L. Y. Li and Z. G. Yang, Recent Progress in Redox Flow Battery Research and Development, *Adv. Funct. Mater.*, 2013, **23**(8), 970–986, DOI: 10.1002/adfm.201200694.
4 M. Skyllas-Kazacos, M. H. Chakrabarti, S. A. Hajimolana, F. S. Mjalli and M. Saleem, Progress in Flow Battery Research and Development, *J. Electrochem. Soc.*, 2011, **158**(8), R55–R79, DOI: 10.1149/1.3599565.
5 A. Z. Weber, M. M. Mench, J. P. Meyers, P. N. Ross, J. T. Gostick and Q. H. Liu, Redox flow batteries: a review, *J. Appl. Electrochem.*, 2011, **41**(10), 1137–1164, DOI: 10.1007/s10800-011-0348-2.
6 J. Noack, N. Roznyatovskaya, T. Herr and P. Fischer, The Chemistry of Redox-Flow Batteries, *Angew Chem Int Edit*, 2015, **54**(34), 9775–9808, DOI: 10.1002/anie.201410823.
7 G. L. Soloveichik, Flow Batteries: Current Status and Trends, *Chem. Rev.*, 2015, **115**(20), 11533–11558, DOI: 10.1021/cr500720t.
8 F. Pan and Q. Wang, Redox Species of Redox Flow Batteries: A Review, *Molecules*, 2015, **20**(11), 20499–20517, DOI: 10.3390/molecules201119711.
9 P. Leung, A. A. Shah, L. Sanz, C. Flox, J. R. Morante, Q. Xu, M. R. Mohamed, C. Ponce de Leon and F. C. Walsh, Recent developments in organic redox flow batteries: A Critical Review, *J. Power Sources*, 2017, **360**, 243–283, DOI: 10.1016/j.jpowsour.2017.05.057.

Open Access Article. Published on 09 December 2025. Downloaded on 4/6/2026 10:10:55 PM. This article is licensed under a Creative Commons Attribution 3.0 Unported Licence.

10 X. L. Wei, W. X. Pan, W. T. Duan, A. Hollas, Z. Yang, B. Li, Z. M. Nie, J. Liu, D. Reed, W. Wang, *et al.*, Materials and Systems for Organic Redox Flow Batteries: Status and Challenges, *ACS Energy Lett.*, 2017, **2**(9), 2187–2204, DOI: 10.1021/acsenergylett.7b00650.

11 J. Winsberg, T. Hagemann, T. Janoschka, M. D. Hager and U. S. Schubert, Redox-Flow Batteries: From Metals to Organic Redox-Active Materials, *Angew. Chem., Int. Ed.*, 2017, **56**, 686–711, DOI: 10.1002/anie.201604925.

12 Y. Ding, C. Zhang, L. Zhang, Y. Zhou and G. Yu, Molecular engineering of organic electroactive materials for redox flow batteries, *Chem. Soc. Rev.*, 2018, **47**, 69–103, DOI: 10.1039/C1037CS00569E.

13 J. A. Luo, B. Hu, M. W. Hu, Y. Zhao and T. L. Liu, Status and Prospects of Organic Redox Flow Batteries toward Sustainable Energy Storage, *ACS Energy Lett.*, 2019, **4**(9), 2220–2240, DOI: 10.1021/acsenergylett.9b01332.

14 K. X. Lin, Q. Chen, M. R. Gerhardt, L. C. Tong, S. B. Kim, L. Eisenach, A. W. Valle, D. Hardee, R. G. Gordon, M. J. Aziz, *et al.*, Alkaline quinone flow battery, *Science*, 2015, **349**(6255), 1529–1532, DOI: 10.1126/science.aab3033.

15 B. Huskinson, M. P. Marshak, C. Suh, S. Er, M. R. Gerhardt, C. J. Galvin, X. D. Chen, A. Aspuru-Guzik, R. G. Gordon and M. J. Aziz, A metal-free organic-inorganic aqueous flow battery, *Nature*, 2014, **505**(7482), 195–198, DOI: 10.1038/Nature12909.

16 A. Hollas, X. L. Wei, V. Murugesan, Z. M. Nie, B. Li, D. Reed, J. Liu, V. Sprenkle and W. Wang, A biomimetic high-capacity phenazine-based anolyte for aqueous organic redox flow batteries, *Nat. Energy*, 2018, **3**(6), 508–514, DOI: 10.1038/s41560-018-0167-3.

17 J. C. Xu, S. Pang, X. Y. Wang, P. Wang and Y. L. Ji, Ultrastable aqueous phenazine flow batteries with high capacity operated at elevated temperatures, *Joule*, 2021, **5**(9), 2437–2449, DOI: 10.1016/j.joule.2021.06.019.

18 T. B. Liu, X. L. Wei, Z. M. Nie, V. Sprenkle and W. Wang, A Total Organic Aqueous Redox Flow Battery Employing a Low Cost and Sustainable Methyl Viologen Anolyte and 4-HO-TEMPO Catholyte, *Adv. Energy Mater.*, 2016, **6**(3), 1501449, DOI: 10.1002/aenm.201501449.

19 P. T. Sullivan, H. Liu, X. L. Lv, S. Jin, W. Li and D. Feng, Viologen hydrothermal synthesis and structure–property relationships for redox flow battery optimization, *Adv. Energy Mater.*, 2023, **13**(34), 2203919.

20 K. X. Lin, R. Gomez-Bombarelli, E. S. Beh, L. C. Tong, Q. Chen, A. Valle, A. Aspuru-Guzik, M. J. Aziz and R. G. Gordon, A redox-flow battery with an alloxazine-based organic electrolyte, *Nat. Energy*, 2016, **1**, 16102, DOI: 10.1038/Nenergy.2016.102.

21 A. Orita, M. G. Verde, M. Sakai and Y. S. Meng, A biomimetic redox flow battery based on flavin mononucleotide, *Nat. Commun.*, 2016, **7**, 13230, DOI: 10.1038/ncomms13230.

22 R. Z. Feng, X. Zhang, V. Murugesan, A. Holias, Y. Chen, Y. Y. Shao, E. Walter, N. P. N. Wellala, L. T. Yan, K. M. Rosso, *et al.*, Reversible ketone hydrogenation and dehydrogenation for aqueous organic redox flow batteries, *Science*, 2021, **372**(6544), 836, DOI: 10.1126/science.abd9795.

23 B. Hu, C. DeBruler, Z. Rhodes and T. L. Liu, Long-Cycling Aqueous Organic Redox Flow Battery (AORFB) toward Sustainable and Safe Energy Storage, *J. Am. Chem. Soc.*, 2017, **139**(3), 1207–1214, DOI: 10.1021/jacs.6b10984.

24 E. S. Beh, D. De Porcellinis, R. L. Gracia, K. T. Xia, R. G. Gordon and M. J. Aziz, A Neutral pH Aqueous Organic-Organometallic Redox Flow Battery with Extremely High Capacity Retention, *ACS Energy Lett.*, 2017, **2**(3), 639–644, DOI: 10.1021/acsenergylett.7b00019.

25 J. Winsberg, C. Stolze, A. Schwenke, S. Muench, M. D. Hager and U. S. Schubert, Aqueous 2,2,6,6-Tetramethylpiperidine-N-oxyl Catholytes for a High-Capacity and High Current Density Oxygen-Insensitive Hybrid-Flow Battery, *ACS Energy Lett.*, 2017, **2**(2), 411–416, DOI: 10.1021/acsenergylett.6b00655.

26 Y. H. Liu, M. A. Goulet, L. C. Tong, Y. Z. Liu, Y. L. Ji, L. Wu, R. G. Gordon, M. J. Aziz, Z. J. Yang and T. W. Xu, A Long-Lifetime All-Organic Aqueous Flow Battery Utilizing TMAP-TEMPO Radical, *Chem-Us*, 2019, **5**(7), 1861–1870, DOI: 10.1016/j.chempr.2019.04.021.

27 J. Luo, M. W. Hu, W. D. Wu, B. Yuan and T. L. Liu, Mechanistic insights of cycling stability of ferrocene catholytes in aqueous redox flow batteries, *Energy Environ. Sci.*, 2022, **15**(3), 1315–1324, DOI: 10.1039/d1ee03251h.

28 L. Hoober-Burkhardt, S. Krishnamoorthy, B. Yang, A. Murali, A. Nirmalchandar, G. K. S. Prakash and S. R. Narayanan, A New Michael-Reaction-Resistant Benzoquinone for Aqueous Organic Redox Flow Batteries, *J. Electrochem. Soc.*, 2017, **164**(4), A600–A60, DOI: 10.1149/2.0351704jes.

29 X. Fang, L. Zeng, Z. Li, L. A. Robertson, I. A. Shkrob, L. Zhang and X. Wei, A cooperative degradation pathway for organic phenoxazine catholytes in aqueous redox flow batteries, *Next Energy*, 2023, **1**(1), 100008, DOI: 10.1016/j.nxener.2023.100008.

30 X. Wei, W. Xu, M. Vijayakumar, L. Cosimbescu, T. Liu, V. Sprenkle and W. Wang, TEMPO-Based Catholyte for High-Energy Density Nonaqueous Redox Flow Batteries, *Adv. Mater.*, 2014, **26**(45), 7649–7653, DOI: 10.1002/adma.201403746.

31 Y. Y. Zhao, J. J. Zhang, G. Agarwal, Z. Yu, R. E. Corman, Y. L. Wang, L. A. Robertson, Z. X. Shi, H. A. Doan, R. H. Ewoldt, *et al.*, TEMPO allegro: liquid catholyte redoxmers for nonaqueous redox flow batteries, *J. Mater. Chem. A*, 2021, **9**(31), 16769–16775, DOI: 10.1039/d1ta04297a.

32 R. K. Gautam, X. Wang, A. Lashgari, S. Sinha, J. McGrath, R. Siwakoti and J. J. Jiang, Development of high-voltage and high-energy membrane-free nonaqueous lithium-based organic redox flow batteries, *Nat. Commun.*, 2023, **14**(1), 4753, DOI: 10.1038/s41467-023-40374-y.

33 T. Janoschka, N. Martin, M. D. Hager and U. S. Schubert, An Aqueous Redox-Flow Battery with High Capacity and Power: The TEMPTMA/MV System, *Angew. Chem., Int. Ed.*, 2016, **55**(46), 14425–14428, DOI: 10.1002/anie.201606472.

34 H. Fan, W. D. Wu, M. Ravivarma, H. B. Li, B. Hu, J. F. Lei, Y. Y. Feng, X. H. Sun, J. X. Song and T. L. Liu, Mitigating Ring-Opening to Develop Stable TEMPO Catholytes for pH-

 This journal is © The Royal Society of Chemistry 2026

Open Access Article. Published on 09 December 2025. Downloaded on 4/6/2026 10:10:55 PM. This article is licensed under a Creative Commons Attribution 3.0 Unported Licence.

Neutral All-organic Redox Flow Batteries, *Adv. Funct. Mater.*, 2022, **32**(33), 2203032, DOI: 10.1002/adfm.202203032.

35 X.-L. Lv, P. T. Sullivan, W. Li, H.-C. Fu, R. Jacobs, C.-J. Chen, D. Morgan, S. Jin and D. Feng, Modular dimerization of organic radicals for stable and dense flow battery catholyte, *Nat. Energy*, 2023, **8**(10), 1109–1118, DOI: 10.1038/s41560-023-01320-w.

36 H. Wang, S. Y. Sayed, E. J. Luber, B. C. Olsen, S. M. Shirurkar, S. Venkatakrishnan, U. M. Tefashe, A. K. Farquhar, E. S. Smotkin, R. L. McCreery, *et al.*, Redox Flow Batteries: How to Determine Electrochemical Kinetic Parameters, *ACS Nano*, 2020, **14**(3), 2575–2584, DOI: 10.1021/acsnano.0c01281.

37 G. te Velde, F. M. Bickelhaupt, E. J. Baerends, C. F. Guerra, S. J. A. Van Gisbergen, J. G. Snijders and T. Ziegler, Chemistry with ADF, *J. Comput. Chem.*, 2001, **22**(9), 931–967, DOI: 10.1002/jcc.1056.

38 B. Hu, Y. J. Tang, J. Luo, G. Grove, Y. S. Guo and T. L. Liu, Improved radical stability of viologen anolytes in aqueous organic redox flow batteries, *Chem. Commun.*, 2018, **54**(50), 6871–6874, DOI: 10.1039/c8cc02336k.

39 P. M. S. Monk, R. D. Fairweather, M. D. Ingram and J. A. Duffy, Evidence for the product of the viologen comproportionation reaction being a spin-paired radical cation dimer, *J. Chem. Soc. Perkin Trans. I*, 1992, **2**(11), 2039–2041, DOI: 10.1039/P29920002039.

40 M. R. Geraskina, A. S. Dutton, M. J. Juetten, S. A. Wood and A. H. Winter, The Viologen Cation Radical Pimer: A Case of Dispersion-Driven Bonding, *Angew. Chem., Int. Ed.*, 2017, **56**(32), 9435–9439, DOI: 10.1002/anie.201704959.

41 J. Huang, Z. Yang, V. Murugesan, E. Walter, A. Hollas, B. Pan, R. S. Assary, I. A. Shkrob, X. Wei and Z. Zhang, Spatially Constrained Organic Diquat Anolyte for Stable Aqueous Flow Batteries, *ACS Energy Lett.*, 2018, **3**, 2533–2538, DOI: 10.1021/acsenergylett.8b01550.

42 A. Orita, M. G. Verde, M. Sakai and Y. S. Meng, The impact of pH on side reactions for aqueous redox flow batteries based on nitroxyl radical compounds, *J. Power Sources*, 2016, **321**, 126–134, DOI: 10.1016/j.jpowsour.2016.04.136.

43 V. D. Sen and V. A. Golubev, Kinetics and mechanism for acid-catalyzed disproportionation of 2,2,6,6-tetramethylpiperidine-1-oxyl, *J. Phys. Org. Chem.*, 2009, **22**(2), 138–143, DOI: 10.1002/poc.1439.

44 Y. Ma, C. Loyns, P. Price and V. Chechik, Thermal decay of TEMPO in acidic media via an N-oxoammonium salt intermediate, *Org. Biomol. Chem.*, 2011, **9**(15), 5573–5578, DOI: 10.1039/C1OB05475A.

45 W. F. Bailey, J. M. Bobbitt and K. B. Wiberg, Mechanism of the oxidation of alcohols by oxoammonium cations, *J. Org. Chem.*, 2007, **72**(12), 4504–4509, DOI: 10.1021/jo0704614.

46 I. Y. Ponedel'kina, E. A. Khaybrakhmanova and T. V. Tyumkina, Reinvestigation of 2,2,6,6-tetramethylpiperidine-1-oxoammonium mono- and tribromide: From old compounds to new findings, *Results Chem.*, 2021, **3**, 100214, DOI: 10.1016/j.rechem.2021.100214.

47 G. I. Borodkin, I. R. Elanov, M. M. Shakirov and V. G. Shubin, Reaction of Nitrosonium Tetrafluoroborate with Nitroxyl Radicals, *Russ. J. Org. Chem.*, 2003, **39**(8), 1144–1150, DOI: 10.1023/B:RUJO.0000010183.47456.c4.

48 A. D. Bain, Chemical exchange in NMR, *Prog. Nucl. Magn. Reson. Spectrosc.*, 2003, **43**(3), 63–103, DOI: 10.1016/j.pnmrs.2003.08.001.

49 X. Zhao, J.-D. Yang and J.-P. Cheng, Revisiting the Electrochemistry of TEMPOH Analogues in Acetonitrile, *J. Org. Chem.*, 2023, **88**(1), 540–547, DOI: 10.1021/acs.joc.2c02537.

50 G. Tang, W. Wu, Y. Liu, K. Peng, P. Zuo, Z. Yang and T. Xu, Adjusting Hirshfeld charge of TEMPO catholytes for stable all-organic aqueous redox flow batteries, *Nat. Commun.*, 2025, **16**(1), 47, DOI: 10.1038/s41467-024-55244-4.

51 O. Nolte, P. Rohland, N. Ueberschaar, M. D. Hager and U. S. Schubert, Stability of TMA-TEMPO-based aqueous electrolytes for redox-flow batteries, *J. Power Sources*, 2022, **525**, 230996, DOI: 10.1016/j.jpowsour.2022.230996.

52 M. Q. Gao, M. Salla, Y. X. Song and Q. Wang, High-Power Near-Neutral Aqueous All Organic Redox Flow Battery Enabled with a Pair of Anionic Redox Species, *Angew. Chem., Int. Ed.*, 2022, **61**(41), e202208223, DOI: 10.1002/anie.202208223.

53 M. Pan, L. Gao, J. Liang, P. Zhang, S. Lu, Y. Lu, J. Ma and Z. Jin, Reversible Redox Chemistry in Pyrrolidinium-Based TEMPO Radical and Extended Viologen for High-Voltage and Long-Life Aqueous Redox Flow Batteries, *Adv. Energy Mater.*, 2022, **12**(13), 2103478, DOI: 10.1002/aenm.202103478.

54 S. M. Weierbach, R. P. Reynolds, S. M. Stephens, K. V. Vlasakakis, R. T. Ritter, O. M. White, N. H. Patel, E. C. Hayes, S. Dunmire and K. M. Lambert, Chemoselective Oxidation of Thiols with Oxoammonium Cations, *J. Org. Chem.*, 2023, **88**(16), 11392–11410, DOI: 10.1021/acs.joc.2c01097.

55 T. Heurich, Z.-W. Qu, G. Schnakenburg, Y. NejatyJahromy, O. Schiemann, S. Grimme and R. Streubel, Chemistry of Thermally Generated Transient Phosphanoxyl Complexes, *Organometallics*, 2017, **36**(15), 2877–2883, DOI: 10.1021/acs.organomet.7b00347.

56 A. Dijksman, A. Marino-González, A. Mairata i Payeras, I. W. C. E. Arends and R. A. Sheldon, Efficient and Selective Aerobic Oxidation of Alcohols into Aldehydes and Ketones Using Ruthenium/TEMPO as the Catalytic System, *J. Am. Chem. Soc.*, 2001, **123**(28), 6826–6833, DOI: 10.1021/ja0103804.

57 C. DeBruler, B. Hu, J. Moss, J. Luo and T. L. Liu, A Sulfonate-Functionalized Viologen Enabling Neutral Cation Exchange, Aqueous Organic Redox Flow Batteries toward Renewable Energy Storage, *ACS Energy Lett.*, 2018, **3**(3), 663–668, DOI: 10.1021/acsenergylett.7b01302.

58 J. Seravalli and S. W. Ragsdale, 13C NMR Characterization of an Exchange Reaction between CO and CO2 Catalyzed by Carbon Monoxide Dehydrogenase, *Biochemistry-Us*, 2008, **47**(26), 6770–6781, DOI: 10.1021/bi8004522.

59 B. C. Kash, R. J. Gomes and C. V. Amanchukwu, Mitigating Electrode Inactivation during CO2 Electrocatalysis in

Open Access Article. Published on 09 December 2025. Downloaded on 4/6/2026 10:10:55 PM.
This article is licensed under a Creative Commons Attribution 3.0 Unported Licence.

Aprotic Solvents with Alkali Cations, *J. Phys. Chem. Lett.*, 2023, **14**(4), 920–926, DOI: 10.1021/acs.jpclett.2c03498.

60 S. M. Pugh and A. C. Forse, Nuclear magnetic resonance studies of carbon dioxide capture, *J. Magn. Reson.*, 2023, **346**, 107343, DOI: 10.1016/j.jmr.2022.107343.

61 K. Kosswig, Sulfonic Acids, Aliphatic, *Ullmann's Encycl. Ind. Chem.*, 2000, **35**, 1–4, DOI: 10.1002/14356007.a25_503.

62 M. Pan, M. Shao and Z. Jin, Development of organic redox-active materials in aqueous flow batteries: Current strategies and future perspectives, *SmartMat*, 2023, **4**(4), e1198, DOI: 10.1002/smm2.1198.

63 C. DeBruler, B. Hu, J. Moss, X. Liu, J. Luo, Y. Sun and T. L. Liu, Designer two-electron storage viologen anolyte materials for neutral aqueous organic redox flow batteries, *Chem*, 2017, **3**(6), 961–978.

64 M. E. Carrington, L. M. Yi, E. Jónsson and C. P. Grey, Practical flow battery diagnostics enabled by chemically mediated monitoring, *Chem-Us*, 2025, **11**(7), 102543, DOI: 10.1016/j.chempr.2025.102543.

 This journal is © The Royal Society of Chemistry 2026